Journal of Magnetic Resonance 303 (2019) 7–16

Contents lists available at ScienceDirect

Journal of Magnetic Resonance

journal homepage: www.elsevier.com/locate/jmr

Probing diffusion dynamics during hydrate formation by high field NMR relaxometry and diffusometry

Linn W. Thrane [a], Joseph D. Seymour [b,*], Sarah L. Codd [a]

[a] Department of Mechanical and Industrial Engineering, Montana State University, Bozeman, MT 59717, United States
[b] Department of Chemical and Biological Engineering, Montana State University, Bozeman, MT 59717, United States

ARTICLE INFO

Article history:
Received 5 December 2018
Revised 2 April 2019
Accepted 3 April 2019
Available online 4 April 2019

Keywords:
Relaxometry
Diffusometry
Molecular dynamics
Hydrate formation

ABSTRACT

High-field nuclear magnetic resonance (NMR) relaxometry and diffusometry along with magnetic resonance imaging were used to monitor phase transition molecular dynamics during hydrate formation occurring in water droplets dispersed in liquid cyclopentane. 1D T_2 relaxation measurements indicate the extent of hydrate formation as well as a reduction in water droplet size with progression of hydrate growth. MRI intensity maps and T_2 relaxation maps indicate spatially dependent hydrate formation rates due to the heterogeneity of the system. Spectrally resolved diffusion measurements indicate a reduction in the porosity of the hydrate agglomerate as the hydrate shell increases in thickness. A novel signal rise observed in two dimensional T_1-T_2 relaxation correlation experiments indicates complex diffusion dynamics due to coupling between regions with varying relaxation and diffusion. These results indicate the ability to monitor hydrate growth and phase transition molecular dynamics due to evolution of the porous hydrate agglomerate by means of high-field NMR.

1. Introduction

Clathrate hydrates are ice-like crystalline compounds in which hydrocarbon is caged by hydrogen bonded water molecules [1,2]. Hydrates typically form at low temperatures and high pressures, and are of particular interest to the oil- and gas industry due to their potential as a natural gas storage, transportation, and recovery source, and their applications in CO_2 sequestration and separation [3]. However, they are also of major concern to the industry as hydrates tend to agglomerate in oil and natural gas pipelines and have the potential to clog pipelines causing damage [1,4,5]. Hydrates nucleate and grow at the interface of water droplets dispersed in the organic phase where hydrogen bonded water cages combine into larger structures. A more detailed understanding of the kinetics of the phase transitions involved in the nucleation, growth and decomposition process of hydrates is needed to further develop and improve technologies required to exploit the potential of natural gas hydrates [6,7], and to reduce the risk of hydrate blockage in pipelines. One of the main obstacles of investigating the phase transitions involved in hydrate formation is the short time and length scales at which the transitions occur and the opaque nature of the material. Nuclear magnetic resonance (NMR) techniques allow for non-invasive studies of complex opaque structures at microscopic length and timescales and have been used extensively in research on hydrates [8–12]. High field studies have focused on spectroscopy [13–15] using ^{13}C, ^{2}H, ^{129}Xe, and solid-state NMR methods [16]. Other high field applications have used magnetic resonance imaging (MRI) to monitor water-methane hydrate formation rates in porous systems [17,18] and for individual water droplets [19]. NMR relaxation is highly sensitive to the thermodynamic phase of the system (liquid-solid-gas) as well as restrictions in motion that occur in porous systems and is therefore an ideal tool for investigating hydrate formation processes.

MRI has been used to monitor the formation of hydrates as the phase transition from liquid water dispersed in the organic phase to crystalline hydrate clusters that occur in bulk or in porous systems generates signal loss [9,17–23]. Haber et al. [10] used low-field NMR relaxometry to measure water consumption and pulsed field gradient (PFG) NMR techniques to monitor the diameter of the water core within a hydrate shell during model cyclopentane hydrate formation. Kleinberg et al. [12] measured T_2 relaxation distributions using a 2.2 MHz logging tool on the sea floor and Gao et al. [24] obtained ^{2}H relaxation distributions in the lab at 2 MHz. However, to our knowledge, no high-field NMR studies of ^{1}H relaxation and diffusion during controlled hydrate formation have been reported. NMR relaxation and diffusion data provides

* Corresponding author.
E-mail address: jseymour@montana.edu (J.D. Seymour).

https://doi.org/10.1016/j.jmr.2019.04.003
1090-7807/

information on the mesoscale dynamics complementing microscale molecular dynamics simulations and macroscale models.

Model cyclopentane hydrates were used in this work to explore the use of high-field NMR relaxometry and diffusometry to characterize molecular dynamics and aggregation structure evolution during the hydrate phase transition. Cyclopentane was chosen as the organic phase as the thermodynamic conditions for hydrate formation are easy to obtain in the NMR sample and it is well studied. It has a high hydrate-forming equilibrium temperature of 7.7 °C at atmospheric pressure and unreacted cyclopentane gives a strong NMR signal since it is a liquid for the temperature range used in this study (−20 to 4 °C). T_2 relaxation MRI was used to provide information on spatial heterogeneity. One dimensional relaxation experiments along with two dimensional T_1-T_2 relaxation correlation experiments and spectrally resolved diffusion measurements were used to observe and characterize the transition from mobile to restricted dynamics simultaneously for both water and cyclopentane throughout the formation process.

The unique ability of NMR relaxometry and diffusometry to measure molecular motion allows this study to characterize mesoscale phase transition molecular motion during hydrate formation due to evolution of the hydrate agglomerate porous structure. The NMR data provides insight into the rate of formation of the hydrates, size and connectivity of the pore space that the water occupies throughout the formation process, and the nature of the exchange of molecules across the evolving hydrate shell.

2. Background

In order to clearly demonstrate the ability of the NMR measurements to characterize the phase transition dynamics, a model of hydrate formation is considered. In this work, cyclopentane is the organic phase. Cyclopentane hydrates form structure II cages at atmospheric pressure and have a hydrate-forming equilibrium temperature of 7.7 °C [25]. This means hydrates will form at any temperature above the melting temperature of the ice and below 7.7 °C, at which point the hydrates will dissociate. Structure II hydrates consist of 16 small 5^{12} cages with the shape of a pentagonal dodecahedron, and 8 hexakaidecahedral shaped larger $5^{12}6^4$ cages [2]. The hydrate cage structures represent the system microscale with time and length scales of microseconds and nanometers.

When the hydrate formation temperature is reached, initial hydrate nucleation occurs at the water-cyclopentane interface. For this study, the experiments were conducted during warming. Initial hydrate nucleation is a stochastic process often followed by an induction time, which is the time between hydrate nucleation and when the system reaches temperature and pressure conditions that support stable hydrates [26–28]. At this point, the growth of hydrate clusters begins [7]. Early hydrate growth is a rapid process that results in a thin hydrate shell with a highly dendritic structure encapsulating the water droplets and creating a barrier between the water and the organic phase [10,29,30]. Haber et al. observed an increase in hydrate shell thickness and a decrease in water core diameter as the hydrate growth progressed [10]. Rao et al. [29] observed a highly porous shell early on in the hydrate growth phase with a porosity of $\varphi \sim$ 95%, consequently the thin hydrate shell does not pose a significant barrier to mass transport [31,32]. In the first 25 h after the onset of hydrate growth, the porosity of the hydrate shell gradually decreases to below 50% and remains almost constant for a period of time [29]. Towards the end of the hydrate growth (the last ~20 h) the shell gets thicker and becomes less porous as the dendritic structure fills in [10] with a final porosity of $\varphi \sim$ 5% [29]. A model of the progression of the hydrate shell growth is shown in Fig. 1. This is the mesoscale of the system, the porous media formed from agglomeration of hydrate cage clusters with length and time scales of microns and milliseconds. NMR relaxation and diffusion data measures molecular dynamics on this scale and they are shown to be consistent with such a shell growth model.

Another aspect of hydrate formation the NMR data informs is the impact of hydrate inhibitors. Hydrate nucleation and growth can be disrupted by hydrate inhibitors which are used by the oil and gas industry to prevent hydrate plugging in pipelines. The most common types of hydrate inhibitors used today are known as low-dosage hydrate inhibitors (LDHIs) [33]. Two different types of LDHIs were added to the aqueous phase in some of the studies performed in this work to investigate changes in molecular dynamics during hydrate formation evident in the NMR data due to the presence of a hydrate inhibitor. The two types of LDHIs are known as kinetic hydrate inhibitors (KHIs) and anti-agglomerants (AAs) [33]. KHIs act to prevent nucleation and are generally water-soluble polymers with functional groups that can be accommodated into the hydrate cages, thus also resulting in an increased induction time and severely delaying the onset of hydrate growth [33,34]. However, when hydrate formation begins, hydrate clusters will form in the same fashion as in the absence of a LDHI. The AAs generally consist of molecules with a hydrate-philic head group and hydrophobic tails and tend to accumulate at the hydrocarbon-water interface where initial hydrate formation occurs. The hydrate-philic head groups will attach to the surface of the hydrate crystals, while the hydrophobic tails repel the aqueous phase, preventing the formation of new hydrate crystals on that surface [33]. Consequently, the hydrate crystals do not agglomerate and remain small and exist as particles dispersed in the liquid hydrocarbon and aqueous phase.

3. Methods

Cyclopentane hydrates were prepared by crushing distilled water ice in a blender. The ice particles were then sieved to

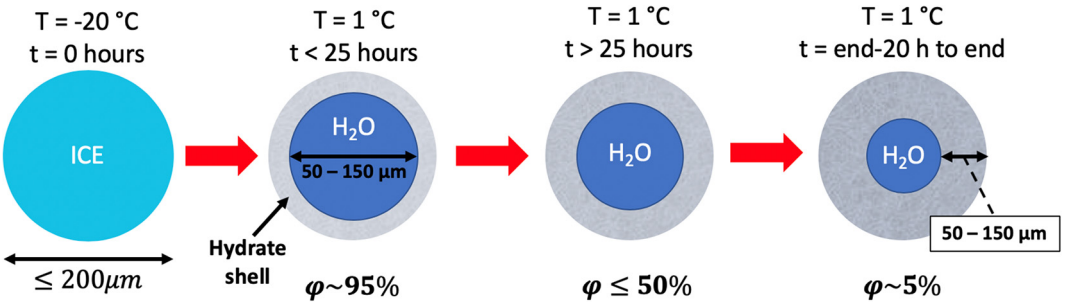

Fig. 1. Once the hydrate nucleation temperature is reached (1 °C in this model), a thin, highly porous hydrate shell will encapsulate the water droplet. Over the first 25 h, the thickness of the shell will increase and gradually fill in, resulting in a decreasing porosity. After the first 25 h, the porosity of the shell stabilizes for a period before it continues to decrease while also continuing to increase in thickness. By the end of the hydrate growth, the porosity has decreased to ~5%. This model is based on the interpretation of work by Haber et al. [10] and Rao et al. [29].

diameters ≤ 250 μm at −20 °C (Montana State University Subzero Research Facility) as thawing ice particles contribute to more rapid hydrate nucleation and more uniform growth [10,35]. Precooled cyclopentane was added in excess to the ice particles using a micro pipette and the mixture was stored in 5 mm NMR test tubes in a Fisher Scientific cooling bath kept at −20 °C. The sample was then transferred to the precooled NMR probe in the magnet bore, also kept at −20 °C. The temperature within the magnet bore was gradually increased at a rate of 1 °C/180 s until the desired melt and nucleation temperature, 1 °C for the data shown here, was reached. This temperature is above the melting temperature of the ice, but below the equilibrium temperature of 7.7 °C for cyclopentane hydrates [25]. Once the desired formation temperature was reached, free induction decays (FID), T_2, T_1-T_2, and diffusion measurements were interleaved until the hydrates reached an equilibrium state and no further hydrate formation occurred. This process took anywhere from 15 to 72 h as monitored by the decrease of the limiting component water spectral peak. In studies where hydrate inhibitors were introduced to the system, the liquid hydrate inhibitor was mixed with the aqueous phase before freezing.

NMR measurements were performed on a Bruker 250 MHz superconducting magnet integrated to an Avance III spectrometer using a high-power rf probe with a 5 mm radio frequency (rf) coil custom built by Bruker. The high-power rf probe integrates with a Diff30 gradient coil capable of z-direction gradients up to 17 T/m at 60 A and allows for rf pulses at 100 W as short as 1 μs. This probe was used to collect T_1 and T_2 relaxation data by performing 1D T_2 experiments and T_1-T_2 correlation experiments, as well as spectrally resolved diffusion data using a pulsed gradient stimulated echo (PGStE) sequence. Spectrally resolved diffusion measurements were performed with pulse length δ = 1 ms, observation time Δ = 300 ms, 64 gradient steps, and a maximum gradient of 0.7 T/m. The PGStE sequence was a mono-polar sequence. The internal gradients were not observed to impact the signal in this system enough to warrant the added complexity and number of phase cycle averages that the Cotts 13 interval bi-polar sequence requires, given the additional time that would be required to acquire a full diffusion data set while the hydrate structure is evolving.

Magnetic resonance imaging (MRI) measurements used a Micro5 gradient coil and probe capable of 3 T/m gradients on all 3 coordinate axes at 60 A. This allowed monitoring of total hydrate formation rate and spatial heterogeneity within the system. A multi-slice multi-echo (MSME) sequence with repetition time TR = 5000 ms, and echo time TE = 7.35 ms was used to obtain relaxation and signal intensity maps of hydrates using 8 echoes. The signal intensity maps were obtained by extrapolating the echo data back to zero time. The sagittal slice has a thickness of 1 mm and a field of view of 5 × 30 mm with 64 × 128 points for a resolution of 0.078 mm/pixel in the x-direction and 0.234 mm/pixel in the z-direction.

T_2 and T_1-T_2 correlation data were acquired using the standard CPMG and inversion recovery pulse sequences with 10 μs rf pulses, echo time of $2 \cdot \tau_2 = 192$ μs, and inversion time τ_1 logarithmically spaced from 1 ms to 50 s. The T_1 and T_2 relaxation times of water and cyclopentane are similar, so to separate the two populations based on relaxation times, a paramagnetic gadolinium complex was added to the cyclopentane. The gadolinium complex, gadolinium tetramethyl heptanedionate (Gd(III) TMHD), is only soluble in the organic phase cyclopentane, and should not impact the relaxation rate of the water [10]. However, the T_1 of water is reduced by the addition of Gd(III)-complex to the cyclopentane (from T_1 = 10 s to T_1 = 1 s), but the T_1 of the water was not further impacted by increased concentration of Gd(III)-complex, suggesting an impact on the water relaxation from Gd-complex at the organic water interface. To determine the concentration of Gd(III) TMHD needed to separate the relaxation rates of the water and the organic phase, the Gd(III) TMHD concentration was gradually increased in increments of ~0.5%. At 0% Gd(III) only one population representing both phases can be seen in the T_1-T_2 correlation map in Fig. 2(a). At 2–2.5% concentration TMHD, the relaxation rates of the two phases were clearly separated as shown in Fig. 2(b), with cyclopentane exhibiting the shorter relaxation times. Full hydrate experiments were run using concentrations of 0.6%, 1.0%, 1.5%, 2.0%, and 2.5%. The concentration of Gd(III) did not impact the formation of hydrate.

4. Results and discussion

T_2 distributions of a hydrate sample with 2.5% Gd(III) TMHD on day 1 and day 4 after the hydrate nucleation temperature of 1 °C was reached are shown in Fig. 3. A shift towards faster relaxation rates is observed for both water and cyclopentane, in agreement

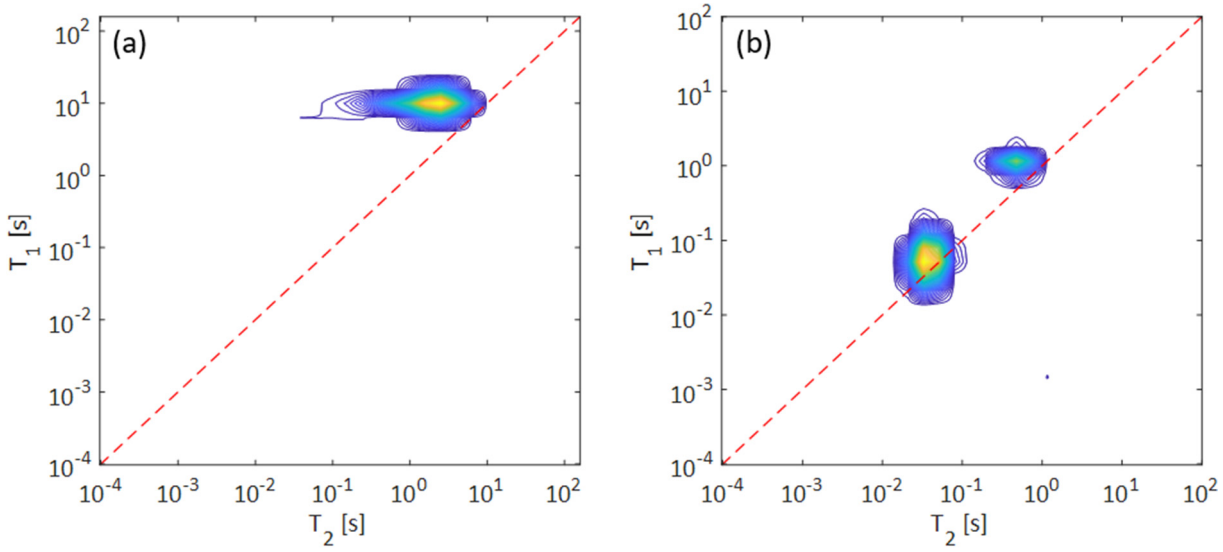

Fig. 2. T_1-T_2 correlation maps for hydrate containing (a) 0% Gd(III) TMHD and (b) 2.5% Gd(III) TMHD. At 0% Gd(III) TMHD, the water and the cyclopentane population cannot be separated based on relaxation rates. At 2.5% Gd(III) TMHD, the relaxation rate of cyclopentane is fast enough that the two populations are clearly separated.

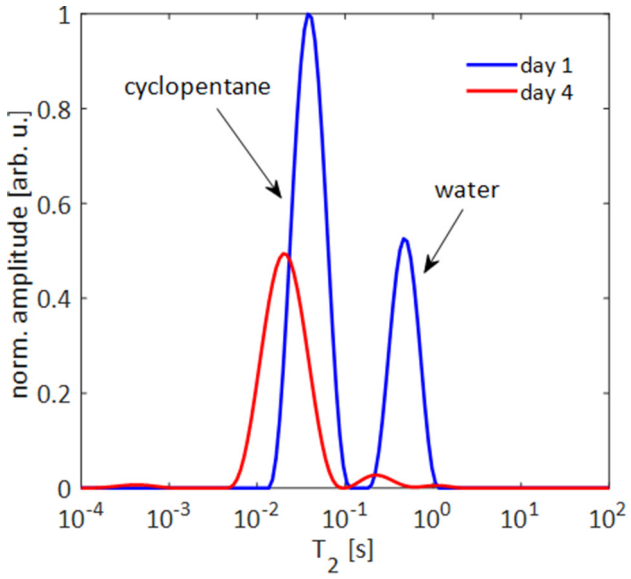

Fig. 3. T_2 distributions of hydrate with 2.5% Gd(III) TMHD on day 1 (blue) and day 4 (red) normalized to the maximum of the cyclopentane peak on day 1. Day 1 is defined as when the nucleation temperature of 1 °C is reached. As the hydrate formation progresses, a shift to shorter T_2 times and a decrease in signal amplitude was observed for both populations. Increase in Gd(III) TMHD concentration causes the shift in T_2 relaxation rate for cyclopentane, while the T_2 shift for water is a result of the water getting more restricted as the hydrate cluster grows. The signal amplitude decreases due to solidification of the water in the hydrate, and single cyclopentane molecules getting trapped in hydrate cages. (For interpretation of the references to color in this figure legend, the reader is referred to the web version of this article.)

with the results obtained at low field by Haber at al. [10] and Gao et al. [24]. The initial T_2 value is ~500 ms for water and ~40 ms for cyclopentane. A shift to shorter T_2 times can be seen for both populations as the hydrate formation progresses, with a final T_2 value of ~200 ms for water and 20 ms for cyclopentane. Additionally, a decrease in signal amplitude with hydrate formation is observed for both water and cyclopentane when the distributions are normalized to the maximum of the cyclopentane peak on day 1. A shift towards shorter T_2 values for water is expected because the liquid water is gradually confined in smaller and smaller spaces as the hydrate formation progresses. The shift to shorter relaxation times for the cyclopentane is attributed to minor changes in gadolinium concentrations over the formation period since the hydrate formation process occurs in the presence of excess cyclopentane. A progressively higher number of cyclopentane molecules get trapped in hydrate cages, leaving a higher ratio of gadolinium to cyclopentane molecules behind to further increase the relaxation rate of the excess cyclopentane. The decrease in signal amplitude is expected as the T_2 relaxation times of water molecules entrained in hydrate cages, and the cyclopentane molecules trapped within these cages, become too short for the NMR equipment to detect. Additionally, the excess cyclopentane was observed to drain towards the bottom if the test tube in some studies. These results agree with previous low-field NMR measurements of a water-cyclopentane [10] and a deuterium water THF [24] hydrate system.

4.1. Frequency spectra

As indicated in the methods, free induction decays (FIDs) were collected throughout the hydrate formation process and Fourier transformed, producing frequency spectra as shown in Fig. 4. Since 13.5 mol of water are consumed for every one mol cyclopentane [1] and the process occurs in the presence of excess cyclopentane, the water frequency peak decreases more rapidly than the cyclopentane peak during hydrate formation. Once the water peak is fully depleted, all of the water is entrained in hydrate cages and no further hydrate nucleation and growth will take place. This state is considered to be the equilibrium state of the hydrate. The variability of the kinetics of the hydrate formation under the same conditions is indicated in Fig. 4(b). While the rates of formation varied from 15 to more than 40 h, the resulting molecular dynamics discussed below were consistently similar.

4.2. Magnetic resonance imaging

Hydrate formation in porous media and in bulk has been studied in detail using MR imaging [9,17–23]. 2D imaging was used to investigate how the heterogeneity of the hydrate samples affect the formation process. Relaxation images were collected to look for variations in relaxation rates across the hydrate sample, and signal intensity images were collected to look for variations in cyclopentane concentration within the ice/cyclopentane mixture. It should be noted that the relaxation measured with the MSME sequence is effective T_2 relaxation due to both surface relaxation and restricted diffusion [36]. Fig. 5 shows a relaxation image and a signal intensity image at −20 °C, where cyclopentane is the only liquid phase in the system. No reaction occurs at this temperature in a cyclopentane/ice system. It can be seen from the relaxation image in Fig. 5(a) that some regions have slower relaxation rates than others, indicating that the liquid cyclopentane in these areas is more restricted. A signal intensity map of the same hydrate at the same temperature can be seen in Fig. 5(b). The different regions are more easily visualized in the relaxation image, Fig. 5(a), because of the low standard deviation of T_2 times within a region, and a 25.6% difference in the average relaxation times between the two regions. The signal intensity (Fig. 5(b)) within the region with shorter relaxation times has a standard deviation that is two times the difference in signal intensity between the two regions, and an average difference in signal intensity of only 5%. Thus, the low difference in signal intensity along with the high standard deviation in the signal intensity map makes it hard to differentiate between regions. However, the 5% difference in signal intensity confirms that the ice particles are more densely packed in regions with shorter T_2 times.

Fig. 6 shows signal intensity maps of a hydrate cluster at 0, 10, and 25 h after the nucleation temperature of 1 °C was reached. At 1 °C, the ice particles start to thaw, and there is both liquid cyclopentane and liquid water present in the system. Yellow regions are areas with high signal and plenty of liquid cyclopentane and water, while dark red regions are areas with hydrate. At 0 h, the signal intensity is high across the entire sample, with liquid water and cyclopentane everywhere. However, as the hydrate formation progresses, the signal intensity decreases, and the previously distinguishable regions reappear, indicating that the hydrates form at a slower rate in some regions of the sample. Due to similarities between Figs. 5 and 6, this spatial variation in the rate of hydrate formation is clearly related to the non-uniform distribution of the ice particles. This initial ice particle packing heterogeneity may cause variation in hydrate formation rate due to higher water droplet concentration, spatial variation in the onset of melting of the ice due to clumping of ice particles, or temperature gradients due to inhomogeneous melting. Hydrate nucleation occurs at water cyclopentane interfaces and is therefore dependent on both interfacial area and the diffusion of the excess cyclopentane to the water interfaces. The cyclopentane/ice surface contact is greater when the ice particles melt while more evenly dispersed throughout the liquid cyclopentane phase. The results confirm that hydrate formation rates have significant variations due to the spatial heterogeneity of the initial distribution of water

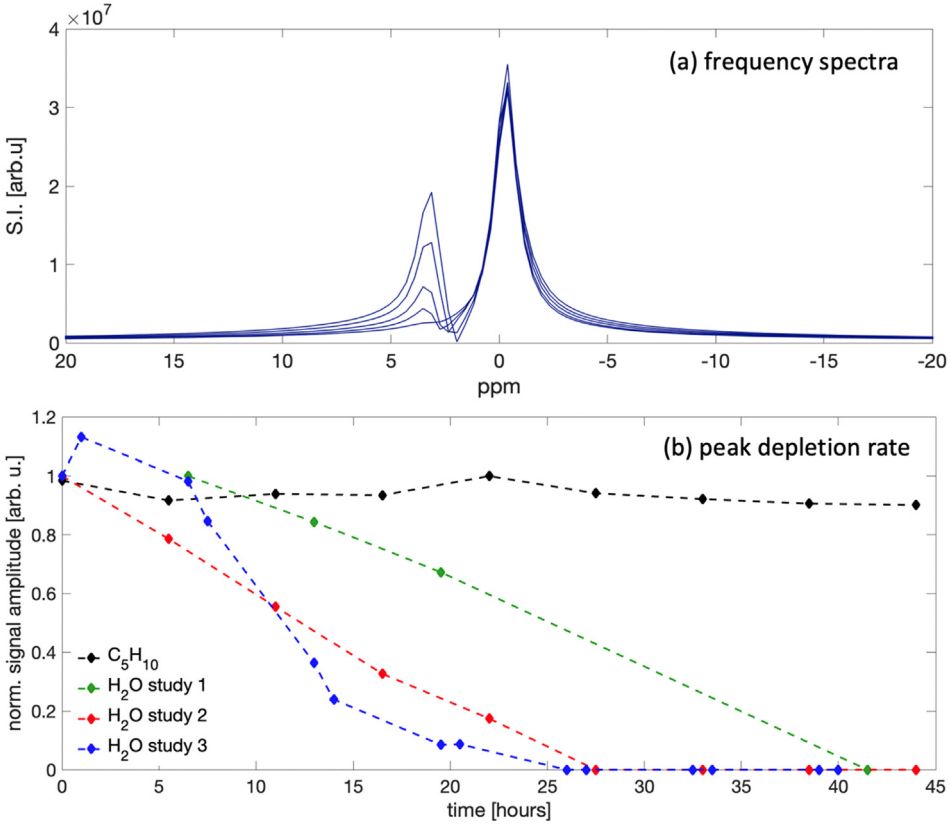

Fig. 4. (a) Frequency spectra showing water (left peak) and cyclopentane (right peak) amplitude throughout the hydrate formation. The water peak disappears due to solidification of the water in the hydrate. (b) Water peak amplitude depletion rate for three different hydrate studies all at 0.6% Gd(III) are shown (study 1 in green, study 2 in red, and study 3 in blue) alongside the time evolution of the cyclopentane peak amplitude (black) for study 2. The plot indicates varying formation rate even in similar systems. The increase in signal in some experiments at 1 h indicates all ice was not melted at t = 0 h. (For interpretation of the references to color in this figure legend, the reader is referred to the web version of this article.)

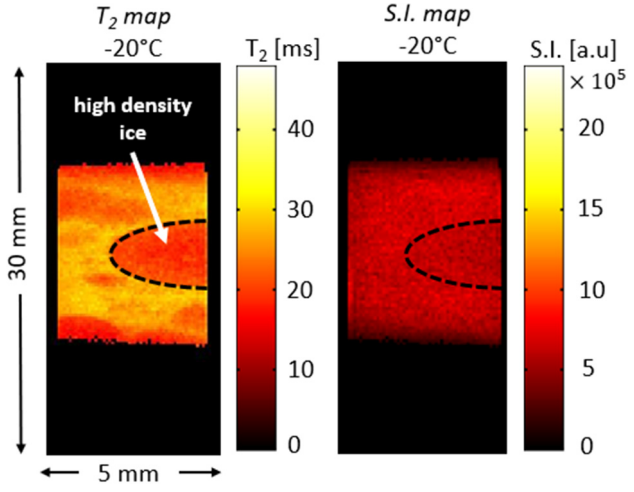

Fig. 5. T_2 relaxation image (a) and signal intensity image (b) at −20 °C before hydrate formation has started. Cyclopentane is the only liquid phase at −20 °C, while water is in the frozen ice phase, thus the uniformity in Fig. 5(b) indicates that the cyclopentane is fairly uniformly (±5%) distributed across the sample. From the relaxation image (a) it can be seen that some regions have faster relaxation rates than others. These darker regions consist of densely packed ice where the liquid cyclopentane is more restricted. The signal intensity image indicates that these darker regions have the same concentration of liquid cyclopentane present on the scale of pixels.

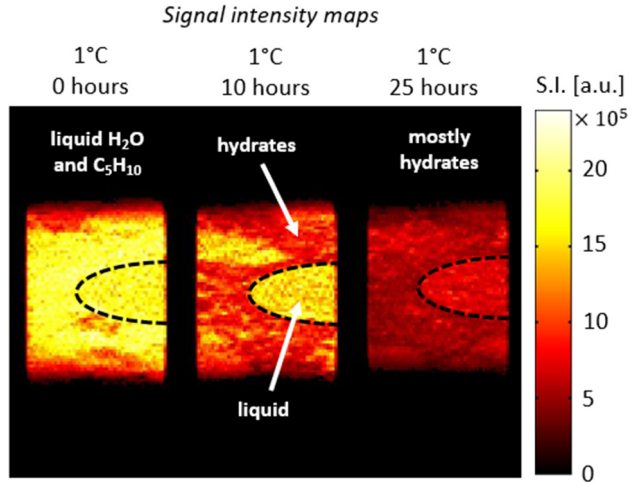

Fig. 6. MR images showing the signal intensity at 0, 10, and 25 h in a hydrate sample as the growth progresses. In these images, the system is at 1 °C, and the liquid phase consist of both cyclopentane and water. At 0 h, the bright yellow color of the S.I. map indicates plenty of liquid water and cyclopentane. As the hydrate formation progresses, the signal intensity across the sample decreases as the water is entrained in hydrate cages. At 25 h, all the water is essentially consumed in the hydrate phase and no longer visible in the S.I. map. The brighter regions at 0 and 10 h therefore demonstrate where water is distributed, and it is clear it is consumed more slowly in some regions such as indicated by the dashed line. (For interpretation of the references to color in this figure legend, the reader is referred to the web version of this article.)

and organic phase within a sample, as observed in a methane-water hydrate system [19].

4.3. Diffusion

As discussed earlier and shown in Fig. 1, following initial hydrate nucleation, a thin layer of hydrate will form a shell around the suspended water droplets [8,10]. With time, the hydrate shell increases in thickness [37]. This reduces the hydrate growth rate due to mass transfer limitations of the excess organic phase cyclopentane to the water interface through the hydrate agglomerate porous media [31,32,37,38]. Mass conservation requires that excess cyclopentane penetrate through the hydrate agglomerate shell, since it is at the liquid water-cyclopentane interface at the interior of the hydrate shell where cages are formed and significantly more water, 13.5 mmol water/1 mmol cyclopentane, is consumed. Spectrally resolved diffusion data indicate two separate diffusion coefficients for water after 6 h of hydrate growth, one fast on the order of 10^{-9} and one slow on the order of 10^{-10} (Fig. 7(a)). The signal attenuation data shown in Fig. 7(a) is biexponential with contributions from both the slow and fast diffusion. The fast diffusion coefficient (1.0×10^{-9} m^2/s) is close to that of free water at 1 °C [39] and is attributed to water in the droplets larger in size than 50 μm as $\Delta = 300$ ms is not long enough to allow significant restricted diffusion impact of water trapped inside the hydrate shell. The slow diffusion coefficient is attributed to the water trapped within the dendritic structure of the porous hydrate shell. The decrease in the slow diffusion coefficient with the progression of hydrate growth indicates a decrease in the pore sizes of the hydrate shell. This can be confirmed by estimating the mean square displacement of hydrogen nuclei in the system given by $\langle \boldsymbol{Z}^2 \rangle = 2D\Delta$, where D is the measured diffusion coefficient, and Δ is the observation time in the PGStE measurement. Fig. 7(b) shows the slow diffusion coefficient decreasing as the hydrate growth progresses. Here, $\Delta = 300$ ms is kept constant for all measurements, thus a decreasing diffusion coefficient results in a decrease in mean square displacement from $\boldsymbol{Z} = \sqrt{2D\Delta}$ of 8.9 μm at 6 hours to 4.8 μm at 69 hours, confirming that the hydrate shell is getting less porous.

The microscale molecular dynamics during hydrate formation have been modeled using classical molecular dynamics simulations [1,4,40] and phase field models [41,42]. These models predict complicated diffusion dynamics due to molecular reorientations and interactions during nucleation and subsequent hydrate growth that occurs on timescales of the order of microseconds (~1 μs) and nanometer length scales (~1 nm) [40]. These molecular reorientation events are occurring constantly throughout the NMR data sampling period. The NMR relaxation and diffusion data provide unique insight into the mesoscale molecular motions associated with hydrate cage agglomeration forming shells around the dispersed water phase droplet and evolution of the agglomerate porous media structure.

The acquired T_1-T_2 correlation data is impacted by these complex diffusion dynamics. In systems with complex diffusion exchange processes the data can exhibit an initial rise in signal in the T_1 dimension whereas an exponential decay is expected in the T_1 dimension in simple systems. This initial rise in signal was first observed by Song *et al.* [43] for water in 150 μm microporous beads. The signal rise is due to complex diffusion dynamics from coupling between pores of varying size and surface relaxivity [43]. The complex diffusion dynamics in the hydrates includes multiple pore sizes, inter-pore diffusion or exchange, and surface relaxation of the cyclopentane within the porous structure formed by the hydrate agglomeration.

Recently we have been developing and extending a coupled pore model [44,45], that demonstrates that a T_1-T_2 signal rise is highly dependent on pore size ratio, pore connectivity, and coupling of relaxation modes. The results of these simulations show that a signal rise is observed for coupling of T_1 and T_2 relaxation modes in a specific combination of the fast and slow diffusion regime, where the fast diffusion regime is defined as $\frac{a\rho_{1,2}}{D} \gg 1$, and the slow diffusion regime is $\frac{a\rho_{1,2}}{D} \ll 1$ [46]. Here, a is the pore diameter, D is the diffusion coefficient, and $\rho_{1,2}$ is the surface relaxivity for the T_1 and T_2 relaxation modes. When mixed mode conditions for fast and slow diffusion regimes are met, an increase in the amplitude of the dominating negative eigenmode is observed. Negative eigenmodes are introduced and described in detail by Song et al. [43,47,48]. These negative amplitude eigenmodes reduce the stability of inverse Laplace transformations [47–49], and are known to reduce the resolution of, and produce $T_1 < T_2$ peaks in T_1-T_2 correlation maps. Consequently, when high amplitude negative eigenmodes are present, T_1-T_2 correlation maps are

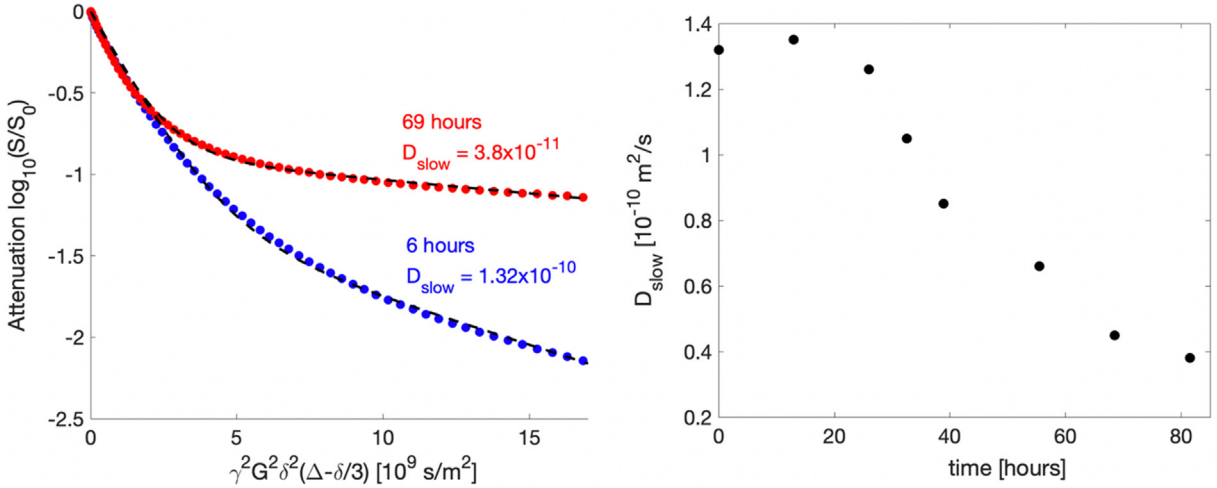

Fig. 7. (a) Stejskal-Tanner plot showing the water phase at 6 (blue) and 69 (red) hours after the onset of hydrate growth. The dashed lines represent the biexponential fit used to obtain the slow diffusion component. At 6 h, a majority of the signal originates from larger droplets of water with a diffusion coefficient at the order of 10^{-9} as indicated by the fast low-q decay. At 69 h, an increase in the ratio of signal originating from water within the porous hydrate shell can be seen. The water trapped in the pore space of the hydrate shell has a diffusion coefficient at the order of 10^{-11}. (b) A decrease in the slower diffusion coefficient with hydrate growth progression is observed. (For interpretation of the references to color in this figure legend, the reader is referred to the web version of this article.)

unreliable. Instead, results should be obtained from the T_1-T_2 time-domain data directly as indicated by Song et al. [43]. The presence of a physical peaks in the ILT is sporadic, dependent on the amplitude of negative eigenmodes [48], so there is no guarantee that aphysical peaks will appear even when the signal rise is robust, thus a signal rise may be present even when no $T_1 < T_2$ peaks are observed in the T_1-T_2 correlation map, emphasizing the importance of observing the more robust time-domain data.

4.4. T_1-T_2 relaxation correlation

In our simulations it appears another requirement for the observed signal rise is an intermediate level of connectivity between the coupled regions. We can denote this connectivity with exchange parameter κ_c If $\kappa_c \to 0$ the regions are completely isolated with no magnetization exchange, and no signal rise is observed. If $\kappa_c \to \infty$, the regions are fully connected, and the system reduces to a single pore system which also does not produce a signal rise. The connectivity between bulk cyclopentane and hydrate agglomerate porous regions in a hydrate system gradually changes throughout the formation process playing a significant role in the T_1-T_2 time domain signal rise observed in the hydrate phase transition dynamics.

During early hydrate formation $\kappa_c \to \infty$ due to the thin and highly porous hydrate shell surrounding the water droplets. Towards the end of the hydrate growth, $\kappa_c \to 0$ as the hydrate shell becomes impermeable. The signal rise observed in the hydrates (Fig. 8(b)) occur exclusively during the intermediate stage of the hydrate formation when the hydrate agglomerate porosity is stable around $\varphi \leq 50\%$ [29]. By the time the water is fully depleted, and the hydrate has reached an equilibrium state, the T_1-T_2 time domain data returns to its usual processed form of an exponential decay (Fig. 8(c)).

Following the early stage of hydrate formation, further hydrate growth along with the exchange of magnetization due to molecular diffusion of cyclopentane between regions of bulk organic phase and pore space within the hydrate agglomerate becomes mass-transfer limited and depends on the diffusivity of the hydrocarbon molecules through the shell as well as the porosity of the shell [38]. The transport of hydrocarbon molecules through the shell is a slow process compared to the frequency at which the NMR signal is collected during T_1-T_2 measurements. Therefore, the effect of the complex diffusion dynamics on the NMR measurements becomes greater with time, as can be seen in the T_1-T_2 time domain data in Fig. 8(b). The initial signal increase becomes more pronounced at longer τ_2-times, since the diffusion exchange between regions of different relaxation and diffusion dynamics occurs at longer τ_2-times [43].

To further investigate the ability of T_1-T_2 relaxation correlation measurements to provide novel data on hydrate formation dynamics, LDHIs were added to the aqueous phase. The first LDHI used, Luvicap® 55 W (provided by BASF, Global Oilfield Solutions), is a KHI which interferes with hydrate nucleation and the formation of hydrate crystals. The second LDHI is an industrial AA (provided by Nalco Champion, Ecolab) which prevents hydrate particles from agglomerating.

The frequency spectra (not shown, data as in Fig. 4) collected during the inhibitor studies show that there was indeed a long delay in the onset of hydrate growth when the KHI was added to the system. The delay was typically 24–48 h relative to the same conditions without KHIs, and no T_1-T_2 signal increase is observed during this initial delay. After 24–48 h, hydrates began to form and a signal rise was again observed during the intermediate stage of the hydrate formation (Fig. 9(a)). As indicated, KHI will delay initial hydrate nucleation, but will not prevent the hydrate crystals from agglomerating once the hydrate growth has started. Hence formation of a porous layer of hydrate agglomerates will occur as a shell around the water droplets suspended in the liquid hydrocarbon phase and an evolving porous media occurs after initial delay, just as in the absence of inhibitors. A signal rise is thus observed in this system as the hydrate formation process is identical to that of hydrates growing in the absence of KHI. In

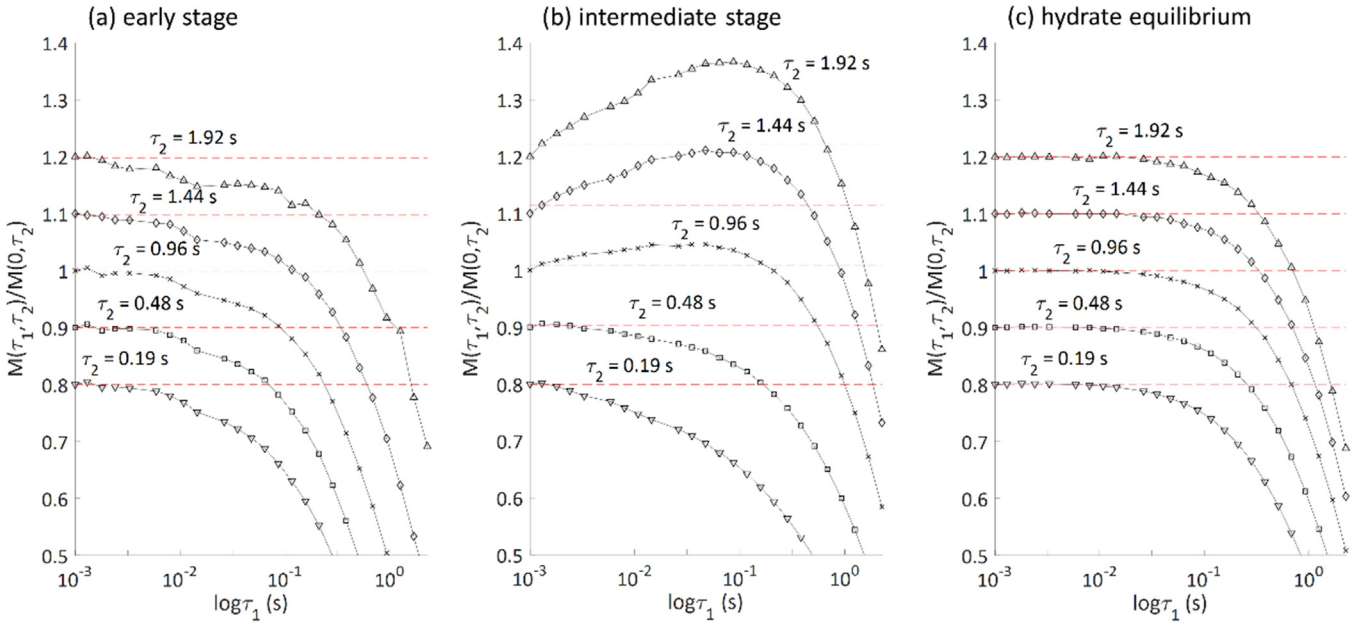

Fig. 8. T_1-T_2 time domain data processed to show exponential decay for ILT analysis. The signal in these plots comes from all liquid water and cyclopentane. (a) Early stage of hydrate formation process at 6 h (b) intermediate stage of hydrate formation process at 14 h, and (c) hydrate equilibrium state at 21 h. An initial increase in signal was observed during the intermediate stage of the hydrate growth process. The data sets are manually shifted vertically at each τ_2 for easier visualization of each individual data set. By the time the hydrate reaches an equilibrium state and hydrate growth was complete, the signal returns to the exponential decaying signal typically observed for processed T_1-T_2 correlation data.

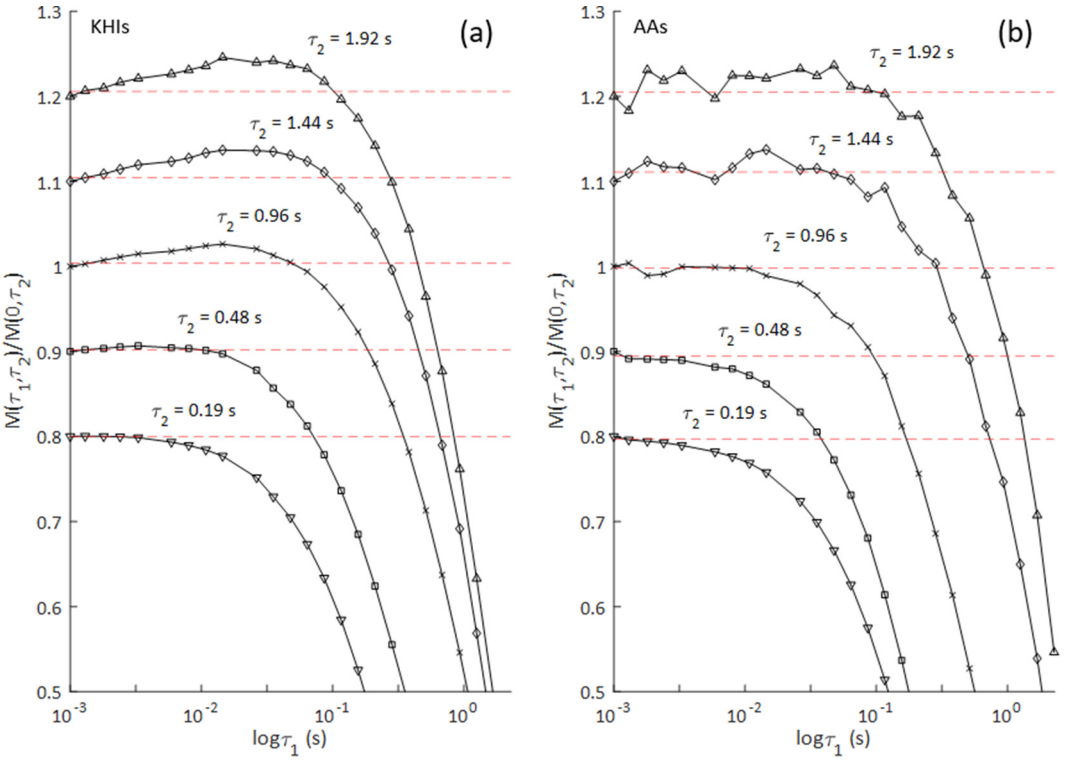

Fig. 9. T_1-T_2 time domain data collected during the intermediate stage of the hydrate formation process in the presence of (a) KHIs and (b) AAs. The signal in these plots comes from all liquid water and cyclopentane. A signal rise was observed in the presence of KHIs due to the fact that KHIs do not disrupt the agglomeration of hydrate crystals, thus a hydrate shell will still form around the water droplets. No signal rise was observed in the presence of AAs. AAs prevent hydrate crystals from agglomerating, resulting in a slurry of fine hydrate particles which do not form a shell encapsulating the water droplets.

the presence of AAs, no signal rise is observed during hydrate formation. Because the AAs prevent hydrate particles from agglomerating, no hydrate shell will form around the water droplets, leaving the hydrate particles dispersed in a slurry of cyclopentane. In the absence of a hydrate shell, there is no restriction to mass transfer between the two phases, and the intermediate level of connectivity required to produce a signal rise according to the coupled pore model is never reached. The additional noise observed at longer τ_2-times in the presence of AAs is a result of a more rapid signal decay (Fig. 10(a)), and therefore a shorter T_2-time, in this system (Fig. 10(b)). The shorter T_2-time is indicative of uniformly dispersed hydrate particles and a lack of larger pockets of liquid as

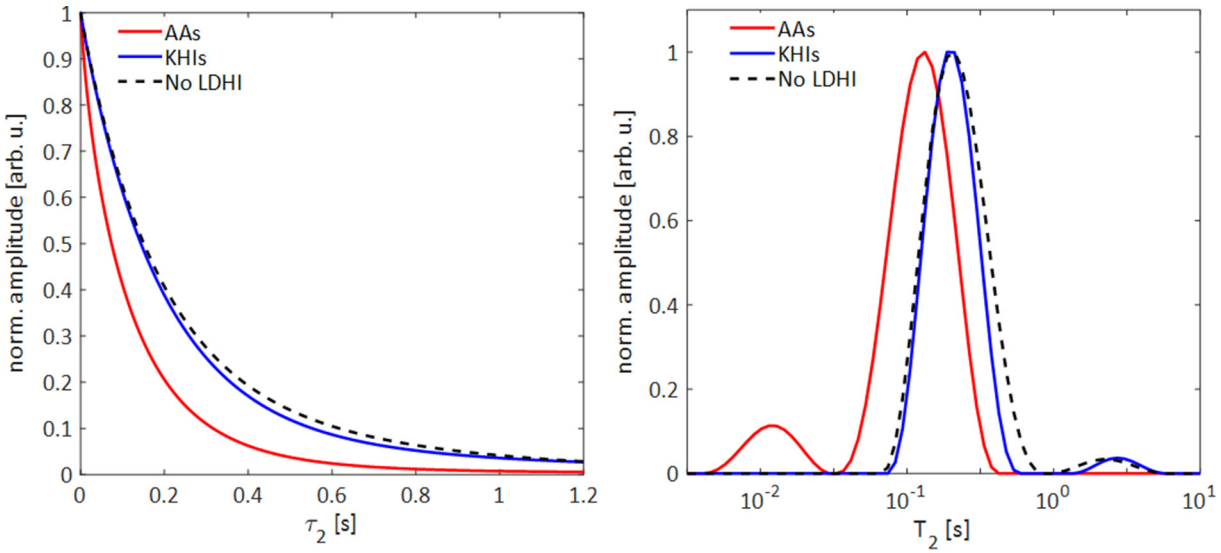

Fig. 10. (a) signal decay in hydrates forming in the presence of KHIs (blue) and AAs (red), and in the absence of a LDHI (black) as a function of τ_2 and (b) corresponding T_2 distributions. In the presence of AAs, a more rapid decay of the NMR signal is observed resulting a shorter T_2 time (~135 ms) compared to the T_2 time (~200 ms) of hydrates forming with KHIs present. The shorter T_2 of hydrates with AAs indicate smaller hydrate particles more uniformly dispersed in cyclopentane. The T_2 time of hydrates with KHI is identical to that of hydrates growing in the absence of a LDHI confirming that the mechanism of the hydrate formation in the presence of KHI is not different once it starts. (For interpretation of the references to color in this figure legend, the reader is referred to the web version of this article.)

those known to exists in hydrate systems without an inhibitor, or in the presence of KHIs. Fig. 10 also confirms the similarity between a hydrate system with KHI and a hydrate system without inhibitors once hydrate formation is initiated in the KHI system.

5. Conclusion

Hydrate formation and growth was detected and monitored by frequency spectra obtained using ^{1}H NMR measurements. Frequency spectra also indicated the hydrate equilibrium state at which point no further hydrate growth was indicated by no further change in the water peak. 1D T_2 distributions show a decrease in peak amplitude for both water and cyclopentane, and a shift to shorter T_2 times for water consistent with low field measurements [10,24]. Water entrained in hydrate cages and cyclopentane molecules trapped within these cages exhibit relaxation times too short to detect due to hardware limitations, thus the decrease in T_2 distribution amplitude indicates the extent of hydrate formation. The decrease in T_2 relaxation time for water indicates a decrease in water droplet size as the hydrate shell surrounding the water droplet increases in thickness. MRI intensity and T_2 relaxation maps indicate spatially dependent hydrate formation rates determined by the density of the packed ice which was heterogeneous. Hydrates grow more rapidly in regions with low ice density due to the increased area of the water-cyclopentane interface. This spatial heterogeneity is related to variations in the rate of hydrate formation observed under the same conditions in the water peak spectra. Spectrally resolved diffusion measurements indicate two distinct diffusion coefficients for the aqueous phase, differing by approximately one order of magnitude. The faster diffusion coefficient is attributed to larger water droplets likely located in regions with high ice density. The slow diffusion coefficient decreases with the progression of hydrate formation, and is attributed to water trapped within the porous hydrate shell. The decrease of the diffusion coefficient indicates a reduction in the pore sizes of the hydrate agglomerate as the hydrate shell increases in thickness.

A novel signal rise is observed in the T_1-T_2 data which indicates that during the intermediate stage of the hydrate growth, when the shell porosity has decreased to $\leq 50\%$, the system consist of two regions, where one region, the trapped water droplets, is in the fast diffusion regime, and the other region, the cyclopentane, is in the slow diffusion regime. The porous hydrate shell determines the connectivity between the two regions and thus controls the existence as well as the amplitude of the signal rise. The data indicates complex diffusion dynamics due to coupling between regions of varying diffusion and relaxation. This research indicates the ability to characterize phase transition molecular dynamics by high-field NMR relaxometry and diffusometry during hydrate formation due to evolution of the hydrate agglomerate porous structure.

Acknowledgements

M. L. Johns, E. O. Fridjonsson, S. J. Vogt, Z. Aman, and N. Ling of Univ. of Western Australia for assistance with hydrate production and materials. J.D.S. and S.L.C. acknowledge the Murdock Charitable Trust for equipment funding and Dieter Gross of Bruker for construction of the high power rf probe. S.L.C. acknowledges funding from NSF CBET-1335534.

References

[1] E.D. Sloan, C.A. Koh, Clathrate Hydrates of Natural Gases, Third Edition., Crc Press-Taylor & Francis Group, Boca Raton, 2008, pp. 1–701.
[2] E.D. Sloan, Fundamental principles and applications of natural gas hydrates, Nature 426 (6964) (2003) 353–359.
[3] I. Chatti et al., Benefits and drawbacks of clathrate hydrates: a review of their areas of interest, Energy Convers. Manage. 46 (9–10) (2005) 1333–1343.
[4] C.A. Koh, Fundamentals and applications of gas hydrates, in: J.M. Prausnitz (Ed.), Annual Review of Chemical and Biomolecular Engineering, Annual Reviews, Palo Alto, 2011, pp. 237–257.
[5] E.G. Hammerschmidt, Formation of Gas hydrates in natural gas transmission lines, Ind. Eng. Chem. 26 (1934) 851–855.
[6] P. Warrier et al., Overview: nucleation of clathrate hydrates, J. Chem. Phys. 145 (21) (2016).
[7] J.A. Ripmeester, S. Alavi, Some current challenges in clathrate hydrate science: nucleation, decomposition and the memory effect, Curr. Opin. Solid State Mater. Sci. 20 (6) (2016) 344–351.
[8] C.P. Aichele et al., Nuclear magnetic resonance analysis of methane hydrate formation in water-in-oil emulsions, Energy Fuels 23 (1) (2009) 835–841.
[9] S.A. Bagherzadeh et al., Magnetic resonance imaging of gas hydrate formation in a bed of silica sand particles, Energy Fuels 25 (7) (2011) 3083–3092.
[10] A. Haber et al., Hydrate shell growth measured using NMR, Langmuir 31 (32) (2015) 8786–8794.
[11] J.A. Ripmeester et al., A new clathrate hydrate structure, Nature 325 (6100) (1987) 135–136.
[12] R.L. Kleinberg et al., Deep sea NMR: Methane hydrate growth habit in porous media and its relationship to hydraulic permeability, deposit accumulation, and submarine slope stability, J. Geophys. Res.-Solid Earth 108 (B10) (2003) 17.
[13] D.W. Davidson, S.K. Garg, J.A. Ripmeester, NMR behavior of clathrate hydrate of tetrahydrofuran. 2. Deuterium measurements, J. Magn. Reson. 31 (3) (1978) 399–410.
[14] J.A. Ripmeester, S.K. Garg, D.W. Davidson, NMR behavior of the clathrate hydrate of tetrahydrofuran. 3. Effect of oxygen, J. Magn. Reson. 38 (3) (1980) 537–544.
[15] T. Pietrass et al., Monitoring xenon clathrate hydrate formation on ice surfaces with optically enhanced Xe-129 NMR, J. Am. Chem. Soc. 117 (28) (1995) 7520–7525.
[16] J.A. Ripmeester, C.I. Ratcliffe, Low-temperature cross-polarization magic angle spinning C-13 NMR of solid methane hydrates – structure, cage occupancy, and hydration number, J. Phys. Chem. 92 (2) (1988) 337–339.
[17] B. Kvamme et al., Storage of CO_2 in natural gas hydrate reservoirs and the effect of hydrate as an extra sealing in cold aquifers, Int. J. Greenhouse Gas Control 1 (2) (2007) 236–246.
[18] J.F. Zhao et al., In-Situ visual observation for the formation and dissociation of methane hydrates in porous media by magnetic resonance imaging, Magn. Reson. Imaging 33 (4) (2015) 485–490.
[19] I.L. Moudrakovski et al., Methane and carbon dioxide hydrate formation in water droplets: spatially resolved measurements from magnetic resonance microimaging, J. Phys. Chem. B 108 (45) (2004) 17591–17595.
[20] B.A. Baldwin, A. Moradi-Araghi, J.C. Stevens, Monitoring hydrate formation and dissociation in sandstone and bulk with magnetic resonance imaging, Magn. Reson. Imaging 21 (9) (2003) 1061–1069.
[21] I.L. Mondrakovski et al., Hydrate layers on ice particles and superheated ice: A H-1 NMR microimaging study, J. Phys. Chem. A 103 (26) (1999) 4969–4972.
[22] R. Susilo et al., Hydrate kinetics study in the presence of nonaqueous liquid by nuclear magnetic resonance spectroscopy and imaging, J. Phys. Chem. B 110 (51) (2006) 25803–25809.
[23] M.J. Yang et al., Advances in nuclear magnetic resonance (NMR) techniques for the investigation of clathrate hydrates, Renew. Sustain. Energy Rev. 74 (2017) 1346–1360.
[24] S.Q. Gao, W.G. Chapman, W. House, Application of low field NMR T-2 measurements to clathrate hydrates, J. Magn. Reson. 197 (2) (2009) 208–212.
[25] M. Nakajima, R. Ohmura, Y.H. Mori, Clathrate hydrate formation from cyclopentane-in-water emulsions, Ind. Eng. Chem. Res. 47 (22) (2008) 8933–8939.
[26] E.D. Sloan et al., Quantifying hydrate formation and kinetic inhibition, Ind. Eng. Chem. Res. 37 (8) (1998) 3124–3132.
[27] D. Kashchiev, A. Firoozabadi, Induction time in crystallization of gas hydrates, J. Cryst. Growth 250 (3–4) (2003) 499–515.
[28] P. Skovborg et al., Measurement of induction times for the formation of methane and ethane gas hydrates, Chem. Eng. Sci. 48 (3) (1993) 445–453.
[29] I. Rao et al., Gas hydrate deposition on a cold surface in water-saturated gas systems, Ind. Eng. Chem. Res. 52 (18) (2013) 6262–6269.
[30] P.U. Karanjkar, J.W. Lee, J.F. Morris, Surfactant effects on hydrate crystallization at the water-oil interface: hollow-conical crystals, Cryst. Growth Des. 12 (8) (2012) 3817–3824.
[31] G. Genov et al., Experimental studies on the formation of porous gas hydrates, Am. Mineral. 89 (8–9) (2004) 1228–1239.
[32] L.T. Chen et al., Methane hydrate formation and dissociation on suspended gas bubbles in water, J. Chem. Eng. Data 59 (4) (2014) 1045–1051.
[33] M.A. Kelland, History of the development of low dosage hydrate inhibitors, Energy Fuels 20 (3) (2006) 825–847.
[34] S.Q. Gao, Hydrate risk management at high watercuts with anti-agglomerant hydrate inhibitors, Energy Fuels 23 (3–4) (2009) 2118–2121.
[35] G. Zylyftari, A. Ahuja, J.E. Morris, Nucleation of cyclopentane hydrate by ice studied by morphology and rheology, Chem. Eng. Sci. 116 (2014) 497–507.
[36] H.T. Edzes, D. van Dusschoten, H. Van As, Quantitative T_2 imaging of plant tissues by means of multi-echo MRI microscopy, Magn. Reson. Imaging 16 (2) (1998) 185–196.
[37] C.J. Taylor et al., Macroscopic investigation of hydrate film growth at the hydrocarbon/water interface, Chem. Eng. Sci. 62 (23) (2007) 6524–6533.
[38] C.Y. Sun et al., The growth kinetics of hydrate film on the surface of gas bubble suspended in water or aqueous surfactant solution, J. Cryst. Growth 306 (2) (2007) 491–499.

[39] R. Mills, Self-diffusion in normal and heavy water in the range 1–45.Deg, J. Phys. Chem. 77 (5) (1973) 685–688.
[40] M.R. Walsh et al., Microsecond simulations of spontaneous methane hydrate nucleation and growth, Science 326 (5956) (2009) 1095–1098.
[41] B. Kvamme et al., Phase field approaches to the kinetic modeling of hydrate phase transitions, in: Natural Gas Hydrates – Energy Resource Potential and Associated Geological Hazards, The American Association of Petroleum Geologists, 2009, pp. 758–769.
[42] G. Tegze, L. Granasy, B. Kvamme, Phase field modeling of CH_4 hydrate conversion into CO_2 hydrate in the presence of liquid CO_2, PCCP 9 (24) (2007) 3104–3111.
[43] Y.Q. Song et al., Experimental identification of diffusive coupling using 2D NMR, Phys. Rev. Lett. 113 (23) (2014) 5.
[44] P.S. Belton, B.P. Hills, The effects of diffusive exchange in heterogeneous systems on NMR line-shapes and relaxation processes, Mol. Phys. 61 (4) (1987) 999–1018.
[45] P.S. Belton, B.P. Hills, The effects of exchange and interfacial reaction in 2-phase systems on NMR lineshapes and relaxation processes, Mol. Phys. 65 (2) (1988) 313–326.
[46] K.R. Brownstein, C.E. Tarr, Importance of classical diffusion in NMR-studies of water in biological cells, Phys. Rev. A 19 (6) (1979) 2446–2453.
[47] Y.Q. Song, L. Zielinski, S. Ryu, Two-dimensional NMR of diffusion systems, Phys. Rev. Lett. 100 (24) (2008) 4.
[48] D. Bytchenkoff, S. Rodts, Structure of the two-dimensional relaxation spectra seen within the eigenmode perturbation theory and the two-site exchange model, J. Magn. Reson. 208 (1) (2011) 4–19.
[49] D.L. Johnson, L.M. Schwartz, Analytic theory of two-dimensional NMR in systems with coupled macro- and micropores, Phys. Rev. E 90 (3) (2014) 032407.